

A POSSIBLE SUPERNOVA REMNANT HIGH ABOVE THE GALACTIC DISK

DAVID B. HENLEY AND ROBIN L. SHELTON

Department of Physics and Astronomy, University of Georgia, Athens, GA 30602

Draft version June 26, 2009

ABSTRACT

We present the analysis of three *Suzaku* observations of a bright arc in the *ROSAT* All-Sky Survey 1/4 keV maps at $l \approx 247^\circ$, $b \approx -64^\circ$. In particular, we have tested the hypothesis that the arc is the edge of a bubble blown by an extraplanar supernova. One pointing direction is near the brightest part of the arc, one is toward the interior of the hypothesized bubble, and one is toward the bubble exterior. We fit spectral models generated from 1-D hydrodynamical simulations of extraplanar supernova remnants (SNRs) to the spectra. The spectra and the size of the arc (radius $\approx 5^\circ$) are reasonably well explained by a model in which the arc is the bright edge of a $\sim 100,000$ -yr old SNR located ~ 1 – 2 kpc above the disk. The agreement between the model and the observations can be improved if the metallicity of the X-ray-emitting gas is $\sim 1/3$ solar, which is plausible, as the dust which sequesters some metals is unlikely to have been destroyed in the lifetime of the SNR. The width of the arc is larger than that predicted by our SNR model; this discrepancy is also seen with the Vela SNR, and may be due to the 1-D nature of our simulations. If the arc is indeed the edge of an extraplanar SNR, this work supports the idea that extraplanar supernovae contribute to the heating of the \sim million-degree gas in the halo.

Subject headings: Galaxy: halo — ISM: bubbles — ISM: supernova remnants — X-rays: diffuse background — X-rays: ISM

1. INTRODUCTION

The discovery of shadows in the 1/4 keV soft X-ray background (SXR) with *ROSAT* demonstrated that there is \sim million-degree gas beyond the Galactic disk, in the Galactic halo (Burrows & Mendenhall 1991; Snowden et al. 1991). Subsequent analysis of data from the *ROSAT* All-Sky Survey (RASS; Snowden et al. 1997), and of spectra from pointed observations with *XMM-Newton* and *Suzaku*, has confirmed the existence of this hot halo gas. Assuming that the gas is in collisional ionization equilibrium (CIE), its temperature is ~ 1 – 3×10^6 K (Snowden et al. 1998; Kuntz & Snowden 2000; Smith et al. 2007; Galeazzi et al. 2007; Henley & Shelton 2008; Lei et al. 2009). High-resolution X-ray absorption line spectroscopy with the *Chandra* gratings also detected hot halo gas (e.g. Yao & Wang 2005). However, despite nearly 20 years of study, a fundamental question about the halo remains: how did the hot gas get there?

Various mechanisms may be contributing to the hot halo gas. One possibility is that the hot gas originated in the disk, heated by stellar winds and supernovae (SNe), and was transferred to the halo via fountains or chimneys (e.g., Shapiro & Field 1976; Norman & Ikeuchi 1989). Another possible source of hot halo gas is gravitational heating of infalling intergalactic material, predicted by simulations of disk galaxy formation (e.g. Toft et al. 2002; Rasmussen et al. 2009). A third possibility, which is the subject of this study, is that the gas is heated *in situ* by SNe above the Galactic disk (Shelton 2006). X-ray spectroscopy is the key to distinguishing between these scenarios. For example, gas that has recently been heated by SNe will be underionized and gas that was heated by SNe in the distant past will be overionized

(e.g., Shelton 1999), while gas that has rapidly expanded out of the disk into the halo will be drastically overionized and recombining (Breitschwerdt & Schmutzler 1994). Also, gas of extragalactic origin may have a different abundance pattern from gas of Galactic origin.

Shelton (2006) considered the soft X-ray emission from an ensemble of isolated supernova remnants (SNRs) of different ages and at different heights above the Galactic plane, taking into account the variation of the SN rate and ambient density as a function of height. She compared this emission to the 1/4 keV (R12) halo emission determined from the RASS. Snowden et al. (1998) decomposed the observed 1/4 keV emission into a foreground component due to the Local Bubble (LB, a cavity in the interstellar medium of radius ~ 100 pc in which the Sun resides, thought to be filled with $\sim 10^6$ K gas), and a distant component, assumed to originate beyond the majority of the Galaxy's H I. This distant component is a combination of halo emission and the extragalactic background. Because the northern Galactic hemisphere contains such anomalous features as the North Polar Spur, and because at low latitudes one cannot clearly see the halo, Shelton (2006) concentrated on high latitudes in the southern Galactic hemisphere. The average de-absorbed count-rate of the distant component for $b < -65^\circ$ is $\sim 800 \times 10^{-6}$ R12 counts $\text{s}^{-1} \text{arcmin}^{-2}$. Subtracting $400 \text{ R12 counts s}^{-1} \text{arcmin}^{-2}$ for the extragalactic background (e.g. Snowden et al. 1998) leaves $\sim 400 \times 10^{-6}$ R12 counts $\text{s}^{-1} \text{arcmin}^{-2}$ for the halo. Shelton (2006) found that up to $\sim 80\%$ of this 1/4 keV flux could be explained by a population of extraplanar SNRs. In this scenario, the vast majority of the flux comes from old SNRs, covering ~ 30 – 90% of the high-Galactic-latitude sky (the fact that they do not cover the whole sky explains the mottled appearance of the 1/4 keV halo emission in the maps of Snowden et al. 1998). However, the individual old SNRs

are rather dim, and so would be difficult to identify.

Shelton (2006) also calculated that $\sim 1\%$ of the high-latitude sky would be covered by young, bright remnants, which should be easier to identify. (Note that in this context, “young” means remnants that are still in the adiabatic phase – their ages could be up to $\sim 10^5$ yr.) This fraction implies that ~ 1 young, bright extraplanar remnant is expected per Galactic hemisphere above $|b| \sim 50^\circ$. SNRs have been found several hundred pc above the plane at low latitudes (e.g., SN 1006 at $z \sim 550$ pc; Winkler et al. 2003), and Shelton et al. (2007) and Lei et al. (2009) have suggested that the X-ray and UV emission from an X-ray-bright region behind a nearby shadowing filament at $l \approx 279^\circ$, $b \approx -47^\circ$ is consistent with the emission from a young remnant. However, to date, no isolated high-latitude extraplanar remnants have been confirmed. Here we examine another promising candidate for a young extraplanar remnant, suggested by Shelton (2006): a bright arc in the RASS 1/4 keV maps (Snowden et al. 1997) at $l \approx 247^\circ$, $b \approx -64^\circ$. This arc is the brightest arc-like feature in the southern Galactic hemisphere below $\sim -40^\circ$, and is shown in Figure 1. The shape of the arc is not due to absorption by intervening material. The right panel of Figure 1 shows the 1/4 keV data overlaid with contours showing the DIRBE-corrected *IRAS* 100- μ m intensity (Schlegel et al. 1998), which traces cool, absorbing material. One can see that there is increased 100- μ m emission (and hence increased absorption of the background X-rays) to the lower left of the arc. However, the absorbing material does not completely follow the edge of the arc, implying that the arc’s shape is not due to absorption.

Although the RASS maps clearly show the presence of the arc, *ROSAT*’s low spectral resolution ($E/\Delta E \sim 1-3$; Snowden et al. 1997) makes detailed studies difficult. Therefore, we have used the X-ray Imaging Spectrometer (XIS; $E/\Delta E \sim 20$ at $E \sim 1$ keV; Koyama et al. 2007) onboard *Suzaku* (Mitsuda et al. 2007) to obtain higher-resolution spectra of the arc and its surroundings, which we used to test Shelton’s (2006) suggestion that the arc is the edge of a young extraplanar SNR. Our three observing directions are shown in the left panel of Figure 1. One observation direction is near the brightest part of the arc (“On arc”), and one is toward the interior of the hypothesized SNR (“Arc interior”). The third observing direction (“Arc background”) is off the arc, outside the hypothesized SNR, and is intended to measure the ambient SXR in the vicinity of the arc. Note that the XIS field of view ($17.8' \times 17.8'$) is much smaller than the radius of the arc ($\sim 5^\circ$), so we cannot obtain data from the entire arc region.

The remainder of this paper is organized as follows. In §2 we describe the *Suzaku* data reduction and spectral extraction. Our first goal is to establish if there are differences in the halo component for our three observation directions. We investigate this question using CIE models, as described in §3. We find that the halo is brighter and slightly cooler in the on-arc direction, compared with the other two directions. This CIE analysis provides a benchmark against which to compare our subsequent analysis, using spectral models based on Shelton’s (2006) hydrodynamical simulations of extraplanar SNRs. This subsequent analysis, described in §4, directly addresses the question of whether or not the arc is the edge of a extra-

planar remnant. In addition, if the arc is the edge of a remnant, our analysis places constraints on the ambient density (corresponding to the height above the disk) and the age of the remnant. We discuss our results in §5. In particular, we assess the SNR hypothesis on the basis of the spectrum, brightness, and gross morphology of the arc (§5.2). We finish with a summary in §6. Throughout we quote 1σ errors.

2. *SUZAKU* DATA REDUCTION

2.1. Initial Data Processing and Cleaning

Table 1 shows the details of our *Suzaku* arc observations. Our data were initially processed at NASA Goddard Space Flight Center (GSFC) using version 2 processing, specifically version 2.0.6.13 for the on-arc observation, version 2.1.6.16 for the arc-interior observation, and version 2.2.11.22 for the arc-background observation. We carried out further data processing using HEASoft¹ version 6.6 and CIAO² version 3.4, following guidelines available from the *Suzaku* Guest Observer Facility at GSFC³. We used the set of calibration database (CALDB) files for the XIS released on 2009 February 03, and the CALDB files for the X-ray Telescope (XRT) released on 2008 July 09. Throughout this paper we used only the data from the back-illuminated XIS1 chip, as it is more sensitive at lower energies than the front-illuminated chips.

We first used the *xispi* tool to update the XIS gain calibration. We then cleaned and filtered the data. We selected events with grades 0, 2, 3, 4, and 6, and used *cleansis* to remove flickering pixels. We excluded the times that *Suzaku* passed through the South Atlantic Anomaly (SAA), times up to 436 s after passage through the SAA, times when *Suzaku*’s line of sight was elevated less than 10° above the Earth’s limb and/or was less than 20° from the bright-Earth terminator, and times when the cut-off rigidity (COR) was less than 8 GV. The thresholds used for the elevation of *Suzaku*’s line of sight above the Earth’s limb and for the COR are higher than the defaults (which are 5° and 6 GV, respectively). The higher elevation threshold reduces contamination from the scattering of solar X-rays off the Earth’s atmosphere, while the higher COR threshold reduces the particle background. We combined the data taken in the 3×3 and 5×5 observation modes, and finally used the CIAO *analyze_ltcsv.sl* script to bin the 2.5–8.5 keV data into 256-s time bins and remove times whose count-rates differ from the mean by more than 3σ . The resulting cleaned XIS1 images are shown in Figure 2.

2.2. Solar Wind Charge Exchange

Observations of the diffuse soft X-ray emission from \sim million-degree Galactic gas may be contaminated by geocoronal and heliospheric solar wind charge exchange (SWCX) emission (Cravens 2000; Cravens et al. 2001; Robertson & Cravens 2003a,b; Koutroumpa et al. 2006, 2007). Periods of enhanced SWCX emission have been associated with periods of increased solar wind proton flux (Cravens et al. 2001; Snowden et al. 2004; Fujimoto et al. 2007).

¹ <http://heasarc.gsfc.nasa.gov/lheasoft>

² <http://cxc.harvard.edu/ciao>

³ <http://suzaku.gsfc.nasa.gov/docs/suzaku/analysis/abc/abc.html>

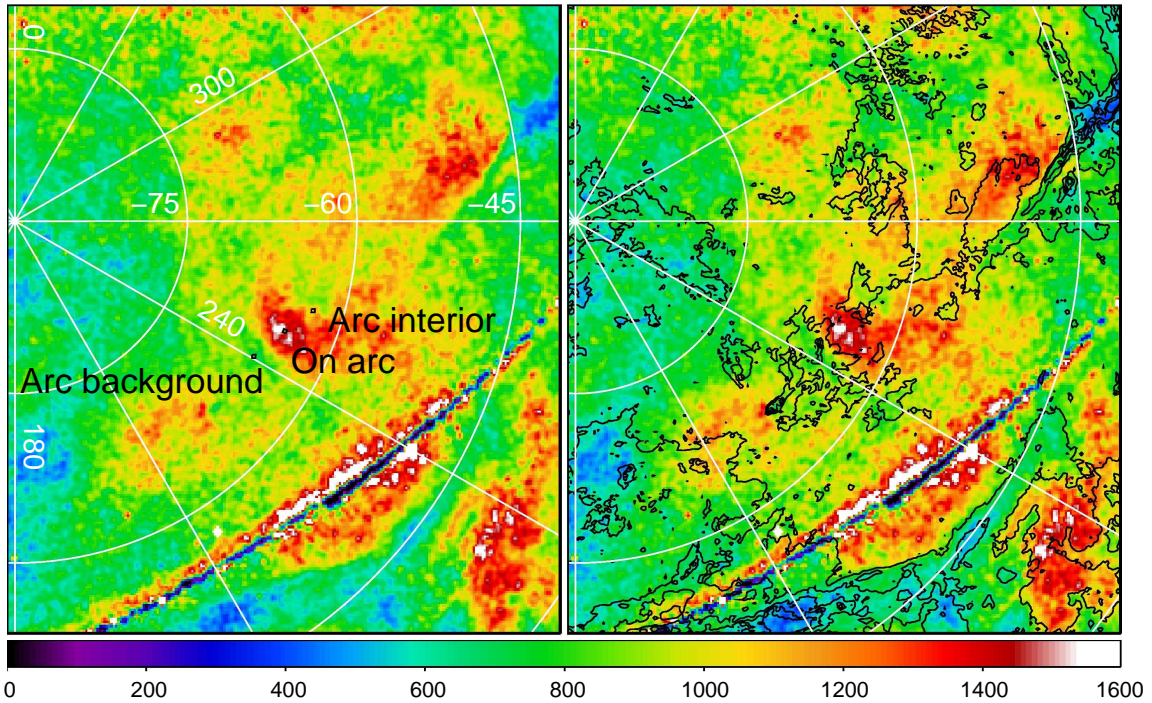


FIG. 1.— *ROSAT* All-Sky Survey 1/4 keV maps of the southern Galactic hemisphere (Snowden et al. 1997), showing the arc that is the subject of this paper. Both panels show the same RASS data, which have been smoothed with a Gaussian whose standard deviation is 2 times the pixel size. The units on the color bar are 10^{-6} counts s^{-1} arcmin^{-2} . The coordinate grid shows Galactic coordinates. The small squares in the left panel show the *Suzaku* XIS field of view ($17.8' \times 17.8'$) for our three pointings (labeled “Arc interior”, “On arc”, and “Arc background”). The contours in the right panel indicate the DIRBE-corrected *IRAS* 100- μm intensity (Schlegel et al. 1998). The contours are at 1, 2, 3, 4, and 5 MJy sr^{-1} .

TABLE 1
DETAILS OF OUR *Suzaku* OBSERVATIONS

Observation	Observation ID	l (deg)	b (deg)	Start time (UT)	End time (UT)	Usable exposure (ks)
Arc interior	502070010	253.29	-62.74	2008-01-15 19:09:14	2008-01-17 18:20:14	74.3
On arc	502071010	247.81	-64.51	2007-06-05 07:29:21	2007-06-07 03:35:19	72.6
Arc background	503104010	240.49	-66.01	2008-12-30 06:07:54	2009-01-04 08:19:23	81.4

Figure 3 compares the 0.3–2.0 keV XIS1 lightcurves for each of our three *Suzaku* observations with the contemporaneous solar wind proton flux obtained from OMNI-Web⁴, which combines solar wind data from several different satellites. In particular, the solar wind data for the arc-interior observation are from the *Advanced Composition Explorer* (*ACE*), those for the on-arc observation are from *ACE* and *Wind*, and those for the arc-background observation are from *Wind*.

In general the solar wind proton flux was fairly steady during our observations. The most notable exception to this statement is the first part of the arc-background observation, when the proton flux was greatly increased. However, there was no significant increase in the soft X-ray count-rate at this time. Despite the steadiness of the X-ray count-rate, we decided to err on the side of caution and removed times when the proton flux exceeded $2 \times 10^8 \text{ cm}^{-2} \text{ s}^{-1}$, or when no solar wind data were available. These times are indicated by the gray datapoints in the lightcurves in Figure 3. The exposure times in Table 1 are those that remain after this additional filtering.

This procedure should help minimize contamination from bright, time-varying geocoronal SWCX. However, it should be noted that it is possible that heliospheric SWCX emission and some quiescent geocoronal SWCX emission still remain in our spectra.

2.3. Point Source Removal

We have previously found that automated source detection software does not work well on *Suzaku* images (Henley & Shelton 2008), presumably because of the broad point spread function. We therefore identified individual sources which may contaminate our diffuse spectra by eye from the 0.3–5.0 keV XIS1 images. Because the tool that we used to calculate non-X-ray background spectra (*xisnxbgen* version 2008-03-08) does not work correctly in sky coordinates, we worked in detector coordinates when identifying and removing individual sources from our XIS1 images. We used circles of radius 115 pixels to exclude the events from around each identified source, except for one bright patch in the arc-background observation, for which we used a radius of 173 pixels. These radii correspond to $\approx 2'$ and $\approx 3'$ on the sky. The positions of the excluded sources are shown in the lower

⁴ <http://omniweb.gsfc.nasa.gov/>

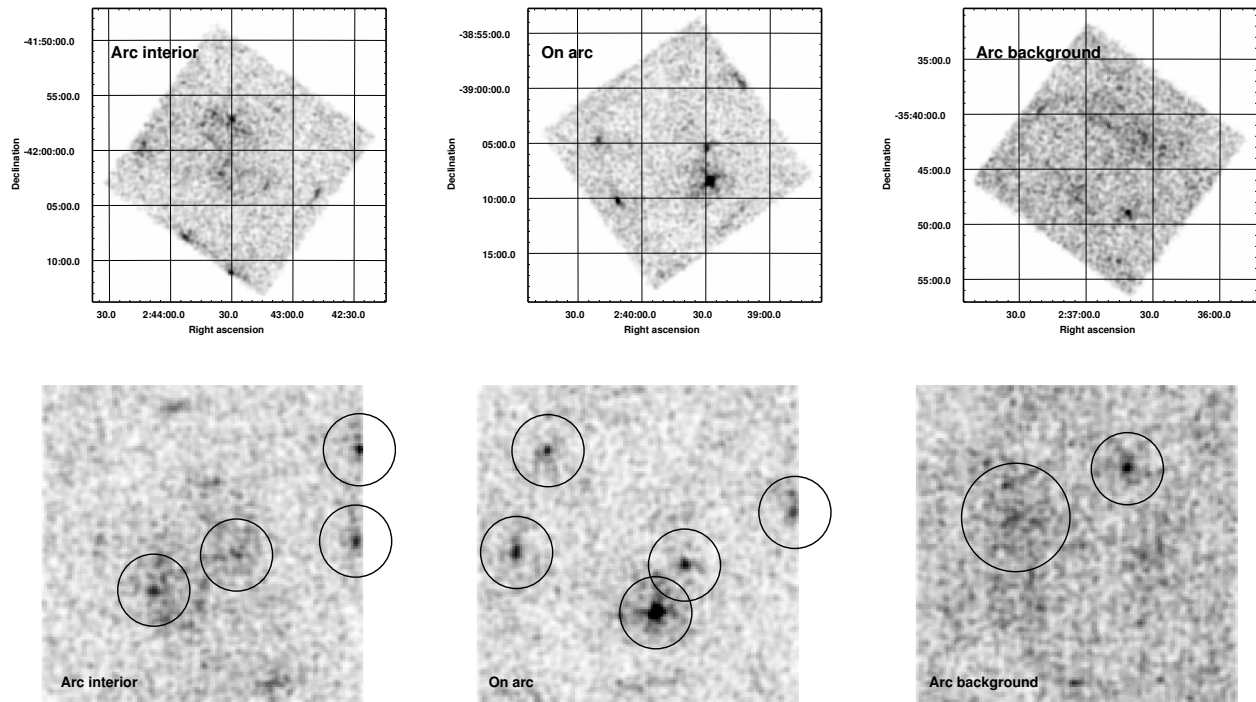


FIG. 2.— Cleaned and smoothed 0.3–5.0 keV XIS1 images from our *Suzaku* arc observations. The upper row of images shows the data in sky coordinates. The lower row of images shows the data in detector coordinates. The black circles outline the regions that were excluded from the analysis – these circles were positioned by eye around sources that might contaminate the spectra of the diffuse emission.

row of Figure 2.

2.4. Spectral Extraction, Non-X-ray Background, and Response Files

We extracted spectra from the full XIS1 field of view, excluding the aforementioned sources and times, and binned the spectra so there were at least 25 counts per bin. We used `xisnxbgen` to calculate non-X-ray background spectra from the database of *Suzaku* night-Earth observations. For each observation we used the same parts of the XIS1 detector to extract the source spectrum and to calculate the non-X-ray background spectrum. We calculated redistribution matrix files (RMFs) using `xisrmfgen`, and ancillary response files (ARFs) using `xissimarfgen`, which takes into account the spatially varying contamination on the optical blocking filters (OBFs) of the XIS sensor (Ishisaki et al. 2007). For the ARF calculations we assumed a uniform source of radius $20'$.

3. SPECTRAL ANALYSIS: EQUILIBRIUM MODEL

In this section we use a simple CIE model to look for variations in the halo emission in the vicinity of the arc. Our CIE model consists of unabsorbed emission from the LB and/or SWCX, absorbed thermal emission from the Galactic halo, and an absorbed power-law for the extragalactic background due to unresolved active galactic nuclei (AGN). The model is described in more detail in §3.1, and the results are presented in §3.2. Although this analysis does not directly address the question of whether or not the arc is the edge of an extraplanar SNR, it establishes parts of the model that we use in our subsequent analysis using SNR models (§4), and it provides a benchmark for comparison with SNR models.

3.1. Model Description

3.1.1. The Foreground Component

When fitting a multicomponent model of the SXR to a spectrum from a single direction, there can be a degeneracy between the foreground (LB/SWCX) and background (halo + extragalactic) emission components. We therefore used Snowden et al.’s (2000) catalog of shadows to fix the normalization of the foreground emission in the vicinity of the arc. This catalog consists of 367 shadows in the $1/4$ keV RASS maps, five of which are in the vicinity of the arc: S2425M653, S2555M621, S2560M560, S2646M675, S2658M582. For each shadow, Snowden et al. (2000) decomposed the *ROSAT* R1 and R2 count-rates into foreground and halo count-rates (with associated errors). In the following test, we found that the foreground count-rates for three of these five shadows could usefully constrain the foreground emission model.

We assumed that the foreground emission could be characterized with a $1T$ CIE plasma model with $T \sim 10^6$ K, as such a model provides a reasonable fit to the *ROSAT* data (Snowden et al. 1998, 2000; Kuntz & Snowden 2000), despite the fact that SWCX emission produces a different spectrum from thermal plasma emission. At first we fitted a $1T$ Raymond & Smith (1977 and updates) model with Anders & Grevesse (1989) abundances to the foreground R1 and R2 count-rates for the five Snowden et al. (2000) shadows near the arc, we obtained a temperature of $(3.8^{+0.3}_{-1.5}) \times 10^6$ K. This foreground temperature is inconsistent with those found by previous studies of the SXR ($T \sim 1.0\text{--}1.3 \times 10^6$ K; Snowden et al. 1998, 2000; Kuntz & Snowden 2000; Galeazzi et al. 2007; Henley & Shelton 2008). In addition, this foreground

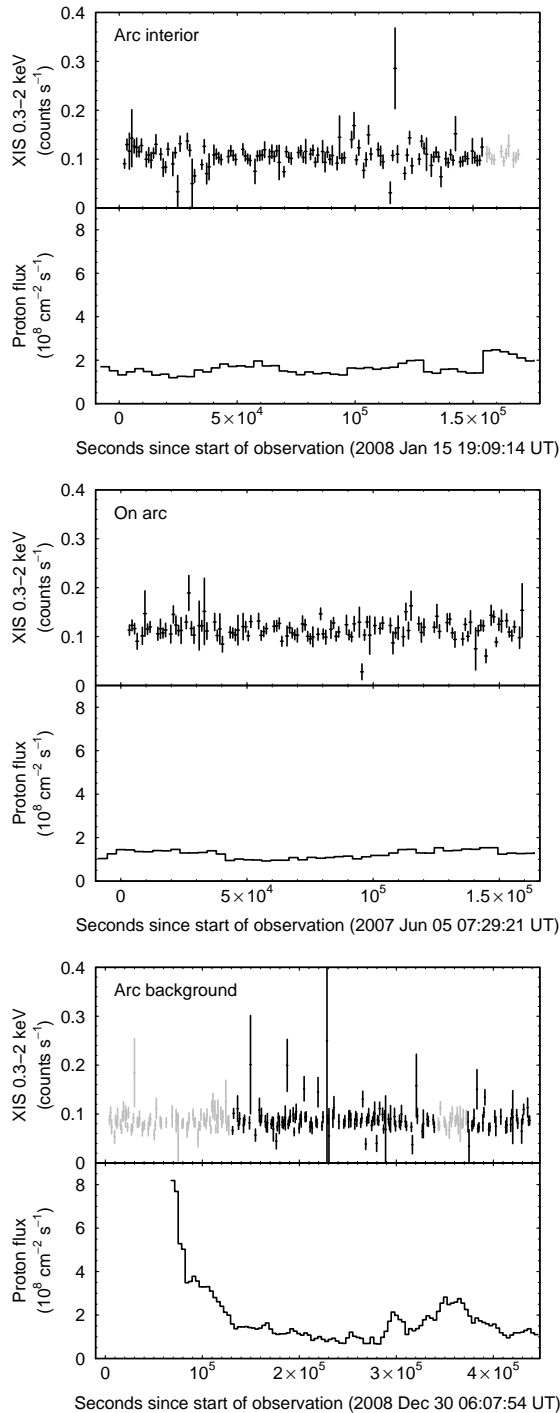


FIG. 3.— XIS1 0.3–2.0 keV lightcurves for each of our three observations, plotted alongside the contemporaneous solar wind proton flux. No solar wind flux data are available for the first ~ 70 ks of the arc-background observation. The gray parts of the lightcurves correspond to times when solar wind data are missing, or when the proton flux exceeded $2 \times 10^8 \text{ cm}^{-2} \text{ s}^{-1}$. These times were removed from the data.

model can be ruled out because it predicts an O VIII Ly α intensity of $\approx 9 \text{ photons cm}^{-2} \text{ s}^{-1} \text{ sr}^{-1}$ (line units, L.U.), which far exceeds what is observed. A closer inspection of the shadows that we used showed that the foreground R2/R1 ratios of two (S2646M675 and S2658M582) are inconsistent with $T \sim 1 \times 10^6 \text{ K}$. When we eliminated these two shadows, we obtained a foreground emission

model with $T = 0.95 \times 10^6 \text{ K}$ and emission measure $\int n_e^2 dl = 0.0041 \text{ cm}^{-6} \text{ pc}$. We used this foreground model in our subsequent *Suzaku* analysis.

3.1.2. The Halo and Extragalactic Components

Although Yao & Wang (2007a) and Lei et al. (2009) have shown that isothermal and two-temperature halo models are inadequate for explaining all the available X-ray and UV emission and absorption data, these models still serve a useful purpose in characterizing the X-ray portion of the emission spectra. Our halo model consisted of a single CIE plasma component (1T model), which was adequate to characterize our data. The temperature and emission measure of the halo component were free parameters in the fitting.

We modeled the extragalactic background as an absorbed power-law. Its photon index was fixed at 1.46 (Chen et al. 1997), but its normalization was a free parameter. So that we could model the attenuation of the halo and extragalactic components, we obtained hydrogen column densities from the Leiden-Argentine-Bonn (LAB) Survey of Galactic H I (Kalberla et al. 2005) using the HEASoft `nh` tool. The hydrogen column densities for our three observing directions are $N_H = 1.9 \times 10^{20} \text{ cm}^{-2}$ (arc interior), $1.6 \times 10^{20} \text{ cm}^{-2}$ (on arc), and $3.6 \times 10^{20} \text{ cm}^{-2}$ (arc background).

3.1.3. Additional Details

In order to better constrain the halo component at lower energies, we included R1 and R2 (1/4 keV) data from the RASS (Snowden et al. 1997). These data were extracted from circles of radius 1° centered on each of our *Suzaku* pointing directions using the `sxrbg` tool available from HEASARC⁵. During the course of our analysis, we discovered a discrepancy between our *Suzaku* spectra and the *ROSAT* R45 (3/4 keV) count-rates – our models significantly underpredict the observed R45 count-rates. We will discuss this discrepancy in §5.1. We decided not to include the R45 data in our spectral analysis. We also did not include the R67 (1.5 keV) data, as this band is dominated by the extragalactic background, and it does not help constrain the Galactic thermal emission.

We used XSPEC⁶ version 11.3.2 (Arnaud 1996) to carry out the spectral analysis. For the thermal plasma components, we used the Astrophysical Plasma Emission Code (APEC) version 1.3.1 (Smith et al. 2001) for the *Suzaku* spectra and the Raymond & Smith (1977 and updates) code for the *ROSAT* R12 data. We used the Raymond & Smith code for the *ROSAT* R12 data because APEC is inaccurate in that band, due to a lack of data on transitions from L-shell ions of Ne, Mg, Al, Si, S, Ar, and Ca.⁷ The parameters of each Raymond & Smith component in the *ROSAT* model were tied to the parameters of the corresponding APEC component in the *Suzaku* model (see Henley & Shelton 2008). For the absorption, we used the XSPEC `phabs` model, which uses cross-sections from Balucińska-Church & McCammon (1992), with an updated He cross-section from Yan et al. (1998). Throughout we used Anders & Grevesse (1989) abundances.

⁵ http://heasarc.gsfc.nasa.gov/Tools/xraybg_help.html#command

⁶ <http://heasarc.gsfc.nasa.gov/docs/xanadu/xspec/xspec11>

⁷ http://cxc.harvard.edu/atomdb/issues_caveats.html

We fitted the model to the 0.3–5.5 keV *Suzaku* + *ROSAT* R12 spectra, with the temperature and emission measure of the halo components and the normalization of the extragalactic background as free parameters. The low-energy cut-off for the *Suzaku* spectra was chosen because the XIS1 calibration is uncertain below 0.3 keV. Although we did not expect much Galactic thermal emission above ~ 1 keV, we included data up to 5.5 keV in order to constrain the extragalactic background. The high-energy cut-off was chosen to avoid the 5.9-keV Mn $K\alpha$ line from the radioactive ^{55}Fe calibration source.

3.2. Results for CIE Models

We fitted our LB/SWCX + 1T halo + extragalactic background model to each of our *Suzaku* + R12 spectra individually. The results are shown in Table 2 and in Figure 4. Generally, the fits are reasonably good. The agreement between the model and the data is also good in the R12 band (not shown). The temperature of the halo is similar in all three directions (~ 0.9 – 1.1×10^6 K). However, the halo emission measure is considerably larger in the on-arc direction – this is not surprising, given that the arc is brighter than its surroundings.

The fact that the halo emission measure is larger in the on-arc direction than the arc-background direction supports statement in the Introduction that the arc’s shape is not due to absorption. If its shape were due to absorption, we would expect the halo to have similar intrinsic intensities in these two directions – this is not what is observed. The halo is slightly cooler in the on-arc direction compared with other two directions, although the difference in temperature is rather small.

Although not relevant to the subsequent discussion, for completeness we note that the normalizations of the extragalactic background in the three directions were 10.6 (arc interior), 9.8 (on arc), and 8.1 (arc background) photons $\text{cm}^{-2} \text{s}^{-1} \text{sr}^{-1} \text{keV}^{-1}$ at 1 keV.

4. SPECTRAL ANALYSIS: SUPERNOVA REMNANT MODELS

The above-described analysis shows that there is intrinsic variation in the halo’s spectrum on and around the arc. However, by itself the above analysis has not helped us address the question of whether or not the arc is the edge of an extraplanar SNR. In this section, we test this hypothesis by fitting spectral models derived from hydrodynamical simulations of extraplanar SNRs (Shelton 2006) to our *Suzaku* + R12 spectra. We look at SNR models with a range of ambient densities (corresponding to different heights above the disk), ambient magnetic fields, and ages. We will assess these models on the basis of the spectrum, brightness and gross morphology of the arc.

The hydrodynamical simulations from which our spectral models are derived are described in §4.1. Our spectral model is described in §4.2. In §4.3 we present the results of the spectral fitting, and we identify the SNR models that are in best agreement with the observations. Finally, in §4.4 we compare the radial surface brightness profile predicted by one of our best-fitting models with the observed *ROSAT* R12 and R45 profiles.

4.1. Hydrodynamical Simulations of Extraplanar Supernova Remnants

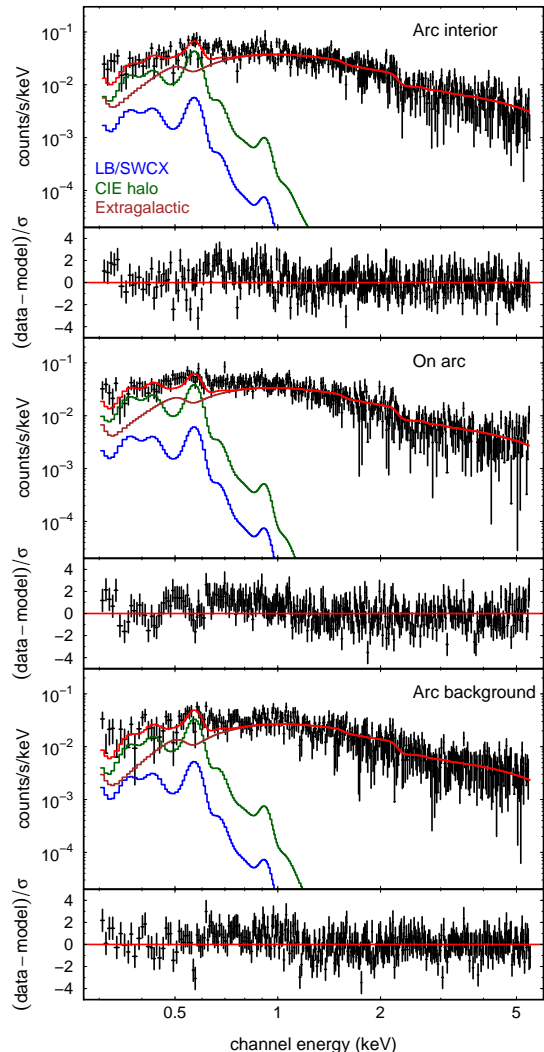


FIG. 4.— Our observed arc-interior, on-arc, and arc-background *Suzaku* XIS1 spectra, plotted with the best-fitting CIE models obtained by fitting to the *Suzaku* + R12 data for each direction individually.

Shelton (2006) carried out 1-D hydrodynamical simulations of extraplanar SNRs in 7 different ambient densities ($n_0 = 0.5, 0.2, 0.1, 0.05, 0.02, 0.01, 0.005 \text{ cm}^{-3}$), corresponding to heights, z , above the midplane ranging from 76 to 1800 pc (using the interstellar density model from Ferrière 1998). For each ambient density, she carried out simulations with $(E_0/10^{51} \text{ erg}, B_{\text{eff}}/\mu\text{G}) = (0.5, 2.5)$ (which we call model type B), $(0.5, 5.0)$ (model type C), and $(1.0, 5.0)$ (model type D), where E_0 is the explosion energy and B_{eff} is the effective magnetic field, which produces a nonthermal pressure in addition to the ambient gas pressure. We have added a fourth type of model, with $E_0 = 0.5 \times 10^{51} \text{ erg}$ and $B_{\text{eff}} = 0$ (model type A). The model parameters are summarized in Table 3 (cf. Table 1 in Shelton 2006). Table 3 gives the conversion between z and n_0 , as well as model IDs that we will use below. The numerical part of the model ID indicates the height of the SNR in pc, while the letter (A–D) indicates E_0 and B_{eff} . The models include thermal conduction, and the ionization evolution in the shocked gas is modeled self-consistently.

TABLE 2
SPECTRAL FIT RESULTS

Observation	Halo T (10^6 K)	Halo E.M. ^a (10^{-3} cm $^{-6}$ pc)	χ^2/dof
Arc interior	1.08 ± 0.02	17.8 ± 0.6	$400.67/346 = 1.16$
On arc	0.95 ± 0.02	$30.0^{+1.0}_{-1.2}$	$394.71/322 = 1.23$
Arc background	1.03 ± 0.02	23.3 ± 1.8	$371.31/339 = 1.10$

^a Emission measure E.M. = $\int n_e^2 dl$ TABLE 3
SNR MODEL PARAMETERS

z (pc)	n_0 (cm $^{-3}$)	E_0 (10^{51} erg)	B_{eff} (μG)	Model ID
76	0.5	0.5	0	76A
	0.5	0.5	2.5	76B
	0.5	0.5	5.0	76C
	0.5	1.0	5.0	76D
190	0.2	0.5	0	190A
	0.2	0.5	2.5	190B
	0.2	0.5	5.0	190C
	0.2	1.0	5.0	190D
310	0.1	0.5	0	310A
	0.1	0.5	2.5	310B
	0.1	0.5	5.0	310C
	0.1	1.0	5.0	310D
480	0.05	0.5	0	480A
	0.05	0.5	2.5	480B
	0.05	0.5	5.0	480C
	0.05	1.0	5.0	480D
850	0.02	0.5	0	850A
	0.02	0.5	2.5	850B
	0.02	0.5	5.0	850C
	0.02	1.0	5.0	850D
1300	0.01	0.5	0	1300A
	0.01	0.5	2.5	1300B
	0.01	0.5	5.0	1300C
	0.01	1.0	5.0	1300D
1800	0.005	0.5	0	1800A
	0.005	0.5	2.5	1800B
	0.005	0.5	5.0	1800C
	0.005	1.0	5.0	1800D

NOTE. — $B_{\text{eff}} = 2.5$ and $5.0 \mu\text{G}$ correspond to non-thermal pressures of 1800 and 7200 cm^{-3} K, respectively.

Figure 5 shows how one such SNR evolves in time. This model is model 1300B in Table 3, and remnant A in Shelton (1999); see that paper for more details. At early times (solid line, $t = 25,000$ yr), the explosion creates a hot cavity or bubble, bounded by the shock. The bubble produces copious soft X-rays – these X-rays come mainly from the hot dense region behind the shock, and the remnant is edge-brightened. As the bubble expands (dotted line, $t = 100,000$ yr), it cools by adiabatic expansion. Nevertheless, the R12 emission remains bright and edge-brightened, although the R45 emission drops considerably. Between $t = 100,000$ and $250,000$ yr (dashed line), the dense rim of the remnant undergoes rapid radiative cooling, forming a cool, dense shell between the edge of the hot bubble at ≈ 100 pc and the shock at ≈ 105 pc. The X-ray count-rate drops considerably after this occurs, although in this case the R12 emission remains edge-brightened. As time goes on, the hot bubble continues to cool (both adiabatically and radiatively)

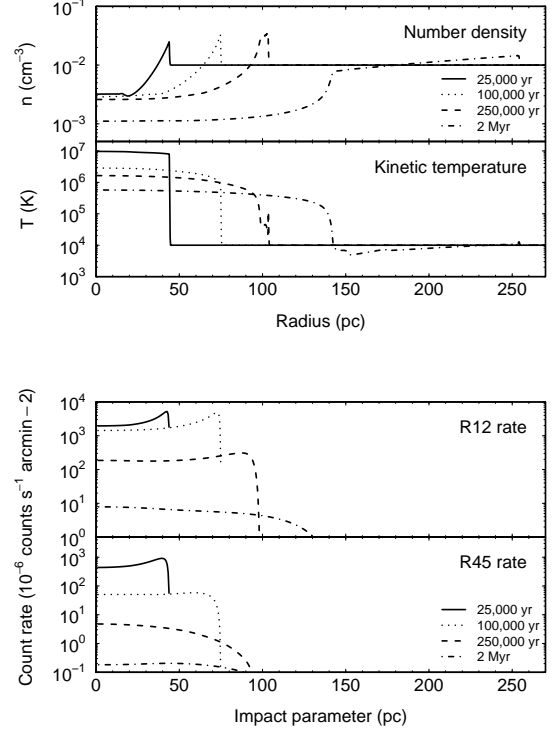


FIG. 5.— The evolution of the density and temperature as a function of radius, and the predicted *ROSAT* R12 and R45 count-rates as a function of impact parameter, for SNR model 1300B (see text for details).

and it gets progressively fainter in X-rays, while the cool shell widens. Eventually, the X-ray emission ceases to be edge-brightened (dot-dash line, $t = 2$ Myr), before the remnant eventually fades away altogether.

Note that the times quoted above are specific to the chosen model – different model parameters (particularly the ambient density) will result in changes on different timescales. For example, a model with $n_0 = 0.5 \text{ cm}^{-3}$ (corresponding to $z = 76$ pc) will form a cool shell between $t = 25,000$ and $50,000$ yr, and the R12 emission will cease to be edge-brightened by $t = 500,000$ yr. However, the general pattern of change described above applies to all the models. As described in the Introduction, Shelton (2006) showed that the combined emission from an ensemble of such SNRs of different ages and at different heights could explain a large fraction of the observed $1/4$ keV halo emission at high Galactic latitudes. Here, we use the results of the SNR simulations summarized in Table 3 to calculate model spectra which we compare with our *Suzaku* + R12 spectra.

4.2. Spectral Model Description

Each simulation dataset consists of hydrodynamical data and ion populations as a function of radius for up to 26 epochs, ranging from $t = 2.5 \times 10^3$ to 2×10^7 yr (the range of ages covered depends on the model). These data were used to calculate X-ray spectra. As the *Suzaku* field of view is much smaller than the size of the arc, we did not calculate spectra for the whole model remnant, but instead calculated projected spectra along various sightlines through the remnant. For this purpose, we used software developed by Shelton (1999), which uses the Raymond & Smith (1977) spectral code (updated by J. C. Raymond & B. W. Smith, 1993, private communication with R. J. Edgar) with abundances from Anders & Grevesse (1989). The spectral calculations take into account the (possibly non-equilibrium) ionization fractions output by the hydrodynamical simulations.

For each epoch of each SNR model, we calculated projected spectra for sight lines through the SNR at various impact parameters (each was measured from the projected center of the remnant). We normalized the model impact parameters such that the normalized value was 0 for a sightline through the center and 1 for a sightline through the part of the rim at which the model R12 count-rate was greatest. For example, for the model shown in Figure 5, the model impact parameters were normalized by dividing by 42.2 pc at $t = 25,000$ yr, and by 72.7 pc at $t = 100,000$ yr. We then used these sets of projected spectra as a function of this normalized impact parameter to create XSPEC table models⁸, one for each epoch of each SNR model.

By eye, we estimated the center of the hypothesized bubble to be at $(l, b) = (256.014^\circ, -61.575^\circ)$ (assuming that the bubble is a circle), while the brightest part of the arc (in the R12 band) is at $(l, b) = (247.90^\circ, -65.09^\circ)$. Therefore, the impact parameters of our on-arc and arc-interior sightlines, normalized to the impact parameter at which the R12 count-rate is greatest, are 0.936 and 0.341, respectively. We used projected SNR spectra calculated for these normalized impact parameters in our spectral analysis.

As in §3, we created a multicomponent emission model consisting of LB/SWCX, halo, and extragalactic components. However, instead of using a 1T CIE model for the halo, we used a SNR + 1T CIE model. The normalization of the brightness of the SNR component was a free parameter, i.e., the brightness of the model SNR emission could be scaled up or down to best match the observed spectrum. If a given SNR model accurately predicts the arc emission, its normalization should be 1. If the spectrum predicted by the SNR component of our multicomponent model is too bright, the SNR model normalization will be less than 1. Similarly, if the model SNR spectrum is too faint, the SNR model normalization will be greater than 1. The normalization of the SNR component was constrained to be the same for the on-arc and arc-interior directions, and was set to zero for the arc-background direction (i.e., we assumed no SNR emission was contributing to the arc-background spectrum). The CIE portion of the halo component was constrained to

be the same in all three directions. As described below, the CIE component is needed to provide adequate fits to the data. This CIE component represents uniform hot halo gas that is not due a young SNR. This hot gas is of unknown origin, and could be due to old SNRs, outflows from the disk, or infalling extragalactic material.

For the LB/SWCX emission, we used the model described in §3.1.1. For the extragalactic background, we again used a power-law with a photon index of 1.46, the normalization of which was independent for each of the three observation directions.

For each epoch of each SNR model, we fitted this LB/SWCX + CIE halo + SNR + extragalactic model to our three *Suzaku* + R12 spectra simultaneously. The free parameters during the fitting were the normalization of the SNR component, the temperature and emission measure of the CIE halo component, and the normalizations of the extragalactic background.

4.3. Results for SNR Models

Here we evaluate our SNR models on the basis of their spectrum (which models give the lowest χ^2 ?), their brightness (which SNR components' normalizations are closest to 1?), and their gross morphology (which models predict an edge-brightened remnant whose radius is close to that of the arc?).

Simultaneously fitting our LB/SWCX + CIE halo + SNR + extragalactic model to our three spectra yielded sets of best-fit parameters as a function of SNR age for each of the 28 SNR models. Figure 6 shows χ^2 as a function of SNR age for a subset of these SNR models. The results plotted are specifically for (a) model type A, with $E_0 = 0.5 \times 10^{51}$ erg and $B_{\text{eff}} = 0$, and (b) model type B, with $E_0 = 0.5 \times 10^{51}$ erg and $B_{\text{eff}} = 2.5 \mu\text{G}$, but the other SNR models produce similar curves. The different curves correspond to SNe exploding at a series of increasing heights (that is, in a series of decreasing ambient densities). Note that not every model epoch yielded a valid fit – at later epochs the model SNR is brightest in the center, whereas the arc (if it is a SNR) is edge-brightened. As a result, not every epoch is shown in the curves in Figure 6. The CIE halo components from these fits have temperatures of $\sim 0.8\text{--}1.1 \times 10^6$ K and emission measures of $\sim 0.015\text{--}0.03 \text{ cm}^{-6} \text{ pc}$. The fits are considerably worse without this component. For example, without a halo component, the arc-background R12 count-rate is significantly underpredicted ($602 \times 10^{-6} \text{ counts s}^{-1} \text{ arcmin}^{-2}$, against an observed count-rate of $(794 \pm 13) \times 10^{-6} \text{ counts s}^{-1} \text{ arcmin}^{-2}$). Without this component, the best-fitting model epochs give $\chi^2 \sim 1600$ for 1012 degrees of freedom, against $\chi^2 \sim 1200$ for 1010 degrees of freedom with the CIE component.

For the lowest height ($z = 76$ pc) there are two minima in the χ^2 curves, corresponding to SNR ages of 50,000 and 150,000 yr. However, for $z \geq 320$ pc, there is a clear single minimum in the χ^2 curves, corresponding to SNR ages of 75,000–100,000 yr. (The exception is the model 1800A, for which the best-fitting age is 250,000 yr.)

The above-described curves tell us which SNR age gives the best fit to the spectra for a given SNR model. However, we would like to further discriminate among the models. To this end, we consider the normalizations of the SNR components, the predicted radii at which the R12 emission is brightest, and χ^2 . Figure 7(a) shows

⁸ <http://xspec.gsfc.nasa.gov/docs/xanadu/xspec/xspec11/manual/nodet.html>

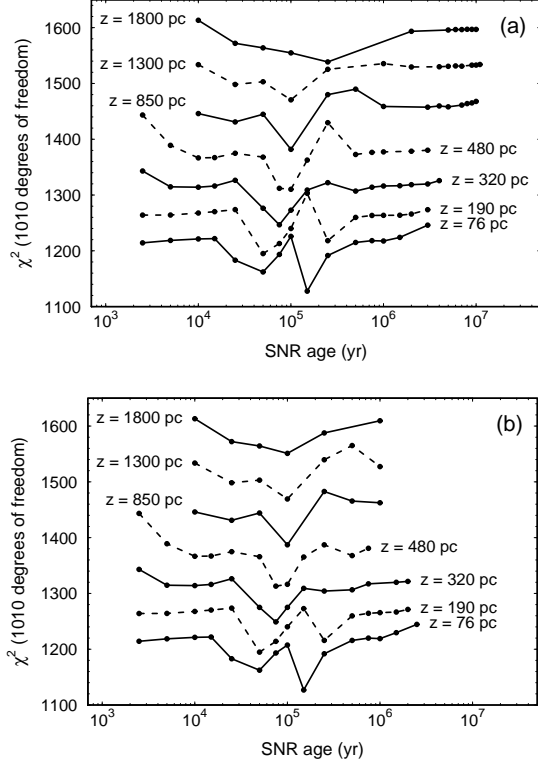


FIG. 6.— Variation of χ^2 with SNR age for SNR models at different heights, z . These results are from fitting the LB/SWCX + CIE halo + SNR + extragalactic model described in §4.2 to our three *Suzaku* + R12 spectra, using (a) SNR model type A ($E_0 = 0.5 \times 10^{51}$ erg, $B_{\text{eff}} = 0$) and (b) SNR model type B ($E_0 = 0.5 \times 10^{51}$ erg, $B_{\text{eff}} = 2.5 \mu\text{G}$). For clarity, the curves for $z = 190, 310, \dots, 1800$ pc have been shifted upward by 50, 100, ..., 300.

the best-fitting normalization of the SNR component for each of the 28 SNR models. As was noted above, if a SNR spectral model accurately represents the arc emission, then its normalization should be 1 – this is shown by a dashed line in the plot. Figure 7(b) shows the predicted radii at which the R12 emission peaks. These radii were calculated for each SNR model using the best-fitting ages. The hydrodynamical simulations give these radii in parsecs. To convert these to angular radii, we calculated the distances to the model SNRs using the nominal heights of the SNR models and assuming a Galactic latitude of -60° . If the center of the hypothesized bubble is at $(l, b) = (256.014^\circ, -61.575^\circ)$ (see above), the observed radius at which the R12 emission peaks is $\approx 5^\circ$ – this is shown by a dashed line in the plot. Figure 7(c) shows the best-fit χ^2 for each model.

For $z = 76$ pc, the best-fitting SNR models are ~ 6 – 12 times too bright, and a factor of ~ 4 too large. For $z = 190$ and 310 pc, the predicted radii are within a factor of 2 of the observed value, but the best-fitting models are ~ 20 – 120 times too bright. The exception is model 190D, which is less than 3 times too bright. However, its predicted radius is 2.5 times too large. For $z = 480$ pc the predicted radii are in very good agreement with the observed value, but the best-fitting models are still an order of magnitude too bright.

The best agreement between the models and the observations is for $z \geq 850$ pc. In terms of the normalization of the SNR component, the models with $E_0 = 0.5 \times 10^{51}$ erg

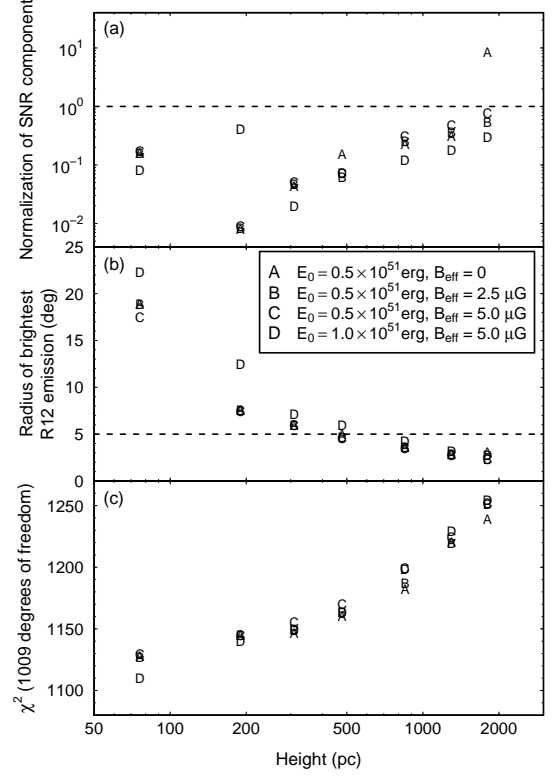


FIG. 7.— The best-fitting (a) normalization of the SNR component, (b) radius of brightest R12 emission, and (c) χ^2 for each of the 28 SNR models that we investigated. The results are plotted as a function of the height of the original SN explosion, corresponding to different ambient densities (see Table 1 in Shelton 2006). The letters A–D denote models with different explosion energies, E_0 , and effective ambient magnetic fields, B_{eff} (see Table 3). The horizontal dashed lines denote a SNR normalization of 1, and a radius of brightest R12 emission of 5° (see text for details). Note that the values of χ^2 are for one fewer degree of freedom than in Figure 6, because for each model we have selected the epoch with the lowest χ^2 .

(model types A, B, and C) are better than those with $E_0 = 1.0 \times 10^{51}$ erg (model type D). The best-fitting $E_0 = 0.5 \times 10^{51}$ erg models are less than a factor of 4.5 too bright, and the radii are within a factor of 2.2 of the observed value (the exception is model 1800A, which is a factor of ~ 10 too faint). Apart from this one model, all models for $z \geq 850$ pc give a best-fitting SNR age of 100,000 yr. However, we cannot easily discriminate among the models for $z \geq 850$ pc with $E_0 = 0.5 \times 10^{51}$ erg, apart from ruling out model 1800A. For example, models 1800B and 1800C have the best-fit SNR normalizations closest to 1, but these models also have larger values of χ^2 than the models for 850 or 1300 pc. Also, at a given height, all the models have similar values of χ^2 .

Figure 8 shows our three *Suzaku* spectra along with the best-fitting spectral model obtained from the SNR model 1300B ($E_0 = 0.5 \times 10^{51}$ erg, $B_{\text{eff}} = 2.5 \mu\text{G}$). This model is in the middle of the range of acceptable heights, and in the middle of the range of magnetic fields used. The model generally does a reasonable job of fitting the spectra (including the R12 data, which are not shown), although the ~ 0.6 – 0.9 keV flux is underpredicted in all three spectra (in the arc-background spectrum, the flux is also underpredicted at lower energies). Over the whole

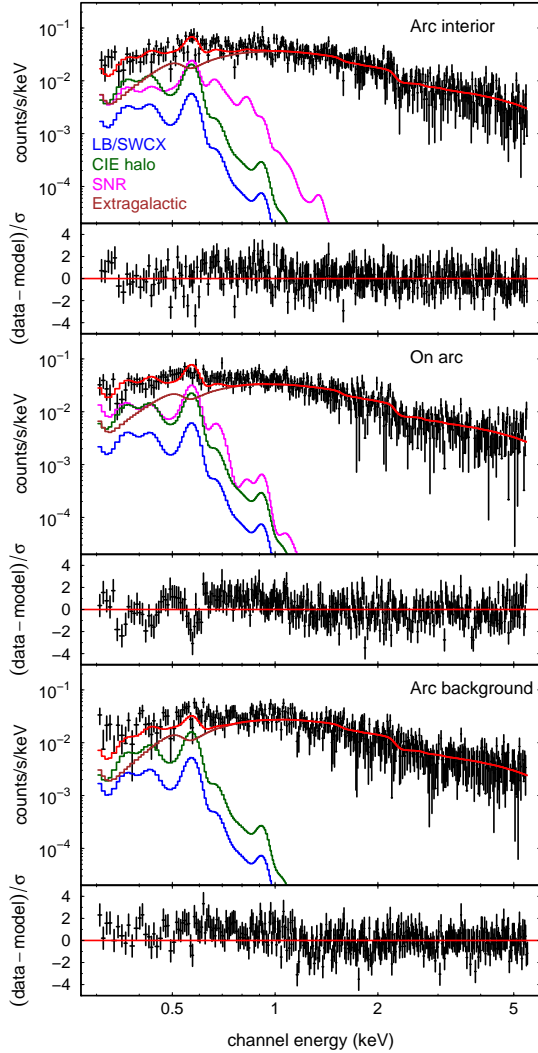


FIG. 8.— The three *Suzaku* spectra with the best-fitting LB/SWCX + CIE halo + SNR + extragalactic model obtained using SNR model 1300B ($E_0 = 0.5 \times 10^{51}$ erg, $B_{\text{eff}} = 2.5 \mu\text{G}$). The individual model components are also plotted.

Suzaku band, the SNR component is brighter in the on arc direction. However, above 0.6 keV the SNR component is brighter in the arc-interior direction, implying that the X-ray emission is harder toward the center of the SNR than toward the edge.

4.4. Comparison of the SNR Model with R12 and R45 Profiles across the Arc

An additional comparison we can make between our model and the observations is to look at profiles of the *ROSAT* R12 and R45 count-rate across the arc. Such a comparison is made in Figure 9, which shows (a) R12 and (b) R45 profiles along a great circle on the celestial sphere starting at the estimated center of the hypothesized SNR at $l = 256.014^\circ$, $b = -61.575^\circ$, and passing over the arc, as near as possible to the three *Suzaku* observations. The model profiles were calculated using the best-fit parameters obtained in the previous section using SNR model 1300B ($E_0 = 0.5 \times 10^{51}$ erg, $B_{\text{eff}} = 2.5 \mu\text{G}$). For each direction along the model profile, we used the column density from Kalberla et al. (2005) calculated us-

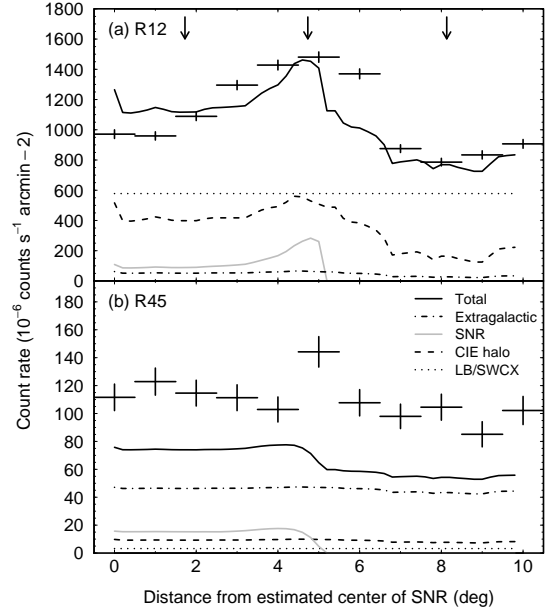


FIG. 9.— Profiles of the observed (a) R12 and (b) R45 count-rates across the arc (crosses) compared with the profile predicted by our best-fitting LB/SWCX + CIE halo + SNR + extragalactic model obtained using SNR model 1300B ($E_0 = 0.5 \times 10^{51}$ erg, $B_{\text{eff}} = 2.5 \mu\text{G}$) (solid line). The individual model components are also plotted. The horizontal axis shows the distance from the estimated center of the hypothesized SNR at $l = 256.014^\circ$, $b = -61.575^\circ$. The arrows show the positions of the three *Suzaku* observations (left to right: arc interior, on arc, arc background).

ing the HEASoft *nh* tool. Although we found some variation in the normalization of the extragalactic background among our three *Suzaku* spectra (see §3.2), we do not know how the extragalactic background varies in the directions between our *Suzaku* observations. Therefore, for the purposes of Figure 9 we assumed a constant value of 9 photons $\text{cm}^{-2} \text{s}^{-1} \text{sr}^{-1} \text{keV}^{-1}$ at 1 keV. The conclusions drawn from Figure 9 are unlikely to be affected by relaxing that assumption.

Figure 9(a) shows that the variation in the model R12 intensity across the arc is due both to the edge-brightened SNR, and to variations in the CIE halo intensity (which are due to variations in N_{H} , as this model component does not vary intrinsically). The model overpredicts the R12 intensity near the center of the hypothesized bubble, and underpredicts the width of the arc.

In the R45 band (Figure 9[b]), the model underpredicts the observed intensity by about a third ($\sim 30\text{--}40 \times 10^{-6} \text{ counts s}^{-1} \text{arcmin}^{-2}$). For the middle data point, the discrepancy is even larger, but this data point may be contaminated by two inaccurately removed point sources (see §5.1, below). The disagreement between the model and the observations shown in Figure 9(b) is not due to a problem with the SNR model itself, but instead is indicative of the general discrepancy between *Suzaku* and the *ROSAT* R45 band already noted in §3.1.3.

5. DISCUSSION

The main goal of this project is to test the hypothesis that the bright arc in the 1/4 keV SXR band at $l \approx 247^\circ$, $b \approx -64^\circ$ is the edge of a bubble blown by an extraplanar SN. In §5.2 below, we will discuss this SNR scenario. However, first we discuss the discrepancy between the

TABLE 4
COMPARING MODEL AND OBSERVED R45
COUNT-RATES

Direction	Model	Observed	
		0.5°	1°
Arc interior	75	109 ± 9	119 ± 5
On arc	69	168 ± 12	122 ± 5
Arc background	55	100 ± 9	95 ± 5

NOTE. — All values are in 10^{-6} R45 counts $\text{s}^{-1} \text{ arcmin}^{-2}$. The observed count-rates were averaged over circles of radius 0.5° and 1°.

Suzaku and *ROSAT* R45 intensities, noted in §§3.1.3 and 4.4.

5.1. The Discrepancy between *Suzaku* and the *ROSAT* R45 Band

As was noted in §3.1.3, during the course of our analysis we discovered a discrepancy between our *Suzaku* spectra and the *ROSAT* R45 (3/4 keV) count-rates. Table 4 compares the R45 count-rates predicted by our *Suzaku* fit results with the observed count-rates, averaged over circles of radius 0.5° and 1°. For the R45 count-rates extracted from the 1° circles, the models underpredict the rates by $\approx 40 \times 10^{-6}$ counts $\text{s}^{-1} \text{ arcmin}^{-2}$ for the arc-interior and arc-background directions, and by 53×10^{-6} counts $\text{s}^{-1} \text{ arcmin}^{-2}$ for the on-arc direction. The on-arc discrepancy increases to 99×10^{-6} counts $\text{s}^{-1} \text{ arcmin}^{-2}$ when we use a 0.5° circle. The SNR model also underpredicts the R45 count-rate (§4.4). The fact that the CIE and SNR models both exhibit this discrepancy implies that the discrepancy is not due to a problem with the SNR model.

Henley & Shelton (2008) also noticed a discrepancy between their *Suzaku* spectra and the corresponding *ROSAT* count-rates. They partially overcame this discrepancy by adding a *vphabs* absorption component to their model. This extra component modeled contamination on the XIS1 optical blocking filter over and above the contamination already included in the CALDB. Henley & Shelton (2008) found that they needed an extra carbon column density of $0.28 \times 10^{18} \text{ cm}^{-2}$, in addition to the CALDB value of $3.1 \times 10^{18} \text{ cm}^{-2}$ at the center of the XIS1 chip. As the systematic uncertainty on the contamination thickness is $\sim 0.5 \times 10^{18} \text{ cm}^{-2}$,⁹ this correction is not unreasonable. However, we were unable to obtain a good fit simultaneously to the *Suzaku*, R12, and R45 data for the on-arc direction, even with an extra *vphabs* absorption component in our model.

We think that the discrepancy may be partly due to the fact that the R45 emission is mottled on scales of $\sim 1^\circ$ (see Figure 10[b]). The observed R45 count-rates are averaged over bright and faint mottled regions. For the on-arc direction, this includes a particularly bright region, which may be partly due to inaccurate removal of the point sources 1RXS J023800.5–390505 and 1RXS J023734.5–391925 (whose positions are shown in Figure 10). Because of the smoothing in Figure 10, and because the size of the XIS field of view is similar to the RASS pixel size ($17.8' \times 17.8'$ versus $12' \times 12'$), one

cannot accurately determine the R45 count-rate in the area exactly corresponding to the XIS field of view. If our *Suzaku* pointings happen to be toward fainter parts of the mottling, while the *ROSAT* count-rates include both bright and faint parts of the mottling, then the *ROSAT* fluxes will be systematically brighter than the *Suzaku* fluxes. In contrast, although the R12 data is much more variable over the whole sky than the R45 data, Figure 10(a) shows that the R12 emission does not seem to be as mottled on small angular scales.

The discrepancy may also be partially due to quiescent SWCX emission that is at a higher level in the *ROSAT* data than in the *Suzaku* data. Variations in the SXR count-rate on a timescale of a few days, referred to as “long-term enhancements” (LTEs), were removed from the RASS data (Snowden et al. 1995). These LTEs are now thought to be due to variations in the heliospheric and/or geocoronal SWCX emission (Cravens et al. 2001). However, even after the LTEs have been removed, a quiescent level of SWCX emission may remain in the data. In the R45 band, this SWCX emission would be dominated by O VII and O VIII emission. At high ecliptic latitudes, such as that of the arc ($\beta \sim -60^\circ$), the heliospheric SWCX emission from these lines is expected to be brighter at solar maximum (such as 1990/1991, when the RASS was carried out) than at solar minimum (when our *Suzaku* observations were carried out) (Koutroumpa et al. 2006). Koutroumpa et al. (2007) give O VII and O VIII intensities for various *Chandra*, *XMM-Newton*, and *Suzaku* observations of the SXR carried out at solar maximum and solar minimum. Using the intensities predicted by their “ground level” model (that is, excluding short-term solar wind enhancements) for the so-called “southern Galactic filament” (SGF), we estimate that the R45 count-rate at high ecliptic latitudes due to quiescent heliospheric SWCX is $\sim 10 \times 10^{-6}$ counts $\text{s}^{-1} \text{ arcmin}^{-2}$ higher at solar maximum than at solar minimum. This could explain $\sim 1/3$ of the discrepancy between *Suzaku* and R45.

Yoshino et al. (2009) compared observed *ROSAT* R45 count-rates with those predicted by *Suzaku* spectra from 14 different directions (1 direction, the North Ecliptic Pole, was observed twice). They found that the *ROSAT* intensities were systematically brighter than the *Suzaku* intensities. For 5 of these directions, the *ROSAT* count-rates may be significantly contaminated by LTEs. After removing these 5 directions, Yoshino et al. (2009) found that the *ROSAT* rates are an average of 17×10^{-6} counts $\text{s}^{-1} \text{ arcmin}^{-2}$ higher than the corresponding *Suzaku* rates. They found that much of this offset could be due to a difference in the point source sensitivity between the two datasets. They also considered variations in the heliospheric SWCX emission between the two datasets.

Figure 11 shows a comparison of the observed *ROSAT* R45 count-rates and the rates predicted by *Suzaku*; the plot shows the results from Yoshino et al. (2009, see their Figure 6) and our arc results. For the purposes of this plot, we re-extracted the observed R45 count-rates using a circle of radius 0.3°, to match Yoshino et al. (2009). As can be seen, the discrepancy that we see for our three spectra is not unusually large when compared with Yoshino et al.’s results.

⁹ <http://heasarc.gsfc.nasa.gov/docs/suzaku/analysis/xis0.html>

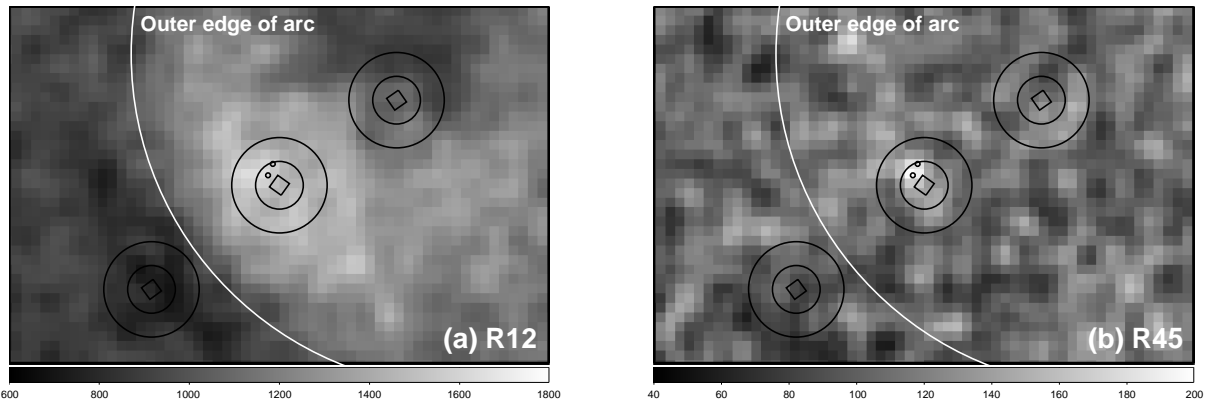


FIG. 10.— Maps of the RASS (a) R12 and (b) R45 count-rate in the vicinity of the arc. The data have been smoothed with a Gaussian whose standard deviation is 2 times the pixel size. The units on the grayscale bar are 10^{-6} counts s^{-1} arcmin $^{-2}$. The squares show the approximate XIS fields of view for our *Suzaku* pointings (top to bottom: arc interior, on arc, arc background). The surrounding circles are of radius 0.5° and 1° . The two smallest circles near the on-arc pointing show the sources 1RXS J023800.5–390505 and 1RXS J023734.5–391925, mentioned in the text. The white line outlines the outer edge of the arc.

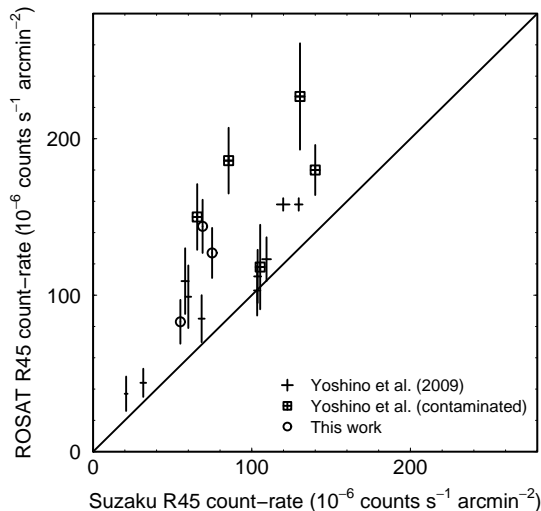


FIG. 11.— Comparison of the R45 count-rates predicted by various *Suzaku* observations with the observed *ROSAT* R45 count-rates (after Yoshino et al. 2009). The crosses show data from Yoshino et al.. The datapoints surrounded by squares are identified by Yoshino et al. as being from possibly contaminated regions of the RASS. Our arc data are shown by open circles. The diagonal solid line shows equality.

Our foreground LB/SWCX model is derived from RASS R12 data (Snowden et al. 2000), and so our foreground model should already include a reasonable estimate of the contamination of the R12 emission by solar maximum heliospheric SWCX emission and unresolved point sources. This model does not make a major contribution in the *Suzaku* band (see Figs. 4 and 8). In addition, as noted above, the R12 data do not seem to be mottled on small angular scales as the R45 data (see Figure 10). We therefore think that our combining the *Suzaku* and R12 data should yield reasonably accurate results.

5.2. Is the Arc the Edge of a Supernova Remnant?

In §4 we used a multicomponent model of the SXR, which include emission from a SNR, to analyze our three *Suzaku* + R12 spectra. In §4.3 we showed that our spectra and the observed size of the arc are reasonably well explained by a model in which the arc is the bright edge

of a $\sim 100,000$ -yr old SNR, blown by a SN explosion with $E_0 = 0.5 \times 10^{51}$ erg at a height of ~ 1 – 2 kpc. (Despite its age, we consider such a SNR to be young, as it is still in the adiabatic stage of its evolution, before the formation of a cool shell.)

It is important to note that the SNR model described in §4 does not fit the spectra better than the CIE models described in §3. As the three fits in Table 2 are completely independent, we can add the values of χ^2 and the degrees of freedom to give $\chi^2 = 1167$ for 1007 degrees of freedom for the CIE model. In contrast, our preferred SNR models give $\chi^2 \approx 1220$ – 1250 for 1009 degrees of freedom. (Note that our two models are not “nested”, so we cannot use the F -test to measure the significance of this difference in χ^2 .) The SNR models appear to do slightly worse in terms of χ^2 , but we point out that the SNR scenario provides a good explanation for the arc’s general morphology.

It should also be noted that there are some discrepancies between the SNR models and the observations: the SNR models are generally either a factor of ~ 3 – 4 too bright or a factor of ~ 2 too small. In addition, the models do not match the observed width of the arc (§4.4). We will first discuss some possible explanations for these discrepancies (§§5.2.1 and 5.2.2), before discussing other possible observations of the arc (§5.2.3).

5.2.1. The Brightness and Size of the Arc

At early epochs, when the model SNRs are still edge-brightened, their X-ray surface brightnesses and physical sizes are most strongly affected by the ambient density, n_0 . As the X-ray emission comes from shock-heated ambient medium, a denser ambient medium gives brighter remnants, as well as hastening the formation of the dense shell. A denser ambient medium also leads to smaller remnants, as in the Sedov phase the radius at a given age is proportional to $n_0^{-1/5}$ (e.g. Spitzer 1978, §12.2b). The apparent size of an object also depends on its distance. In the case of our SNR models, the distance is derived from the height, z , corresponding to the ambient density (Shelton 2006), using a Galactic latitude of -60° .

Model 1800C ($E_0 = 0.5 \times 10^{51}$ erg, $B_{\text{eff}} = 5.0$ μ G, $n_0 = 0.005$ cm $^{-3}$) gives the best result in terms of the SNR surface brightness – of all our SNR models, the

best-fitting normalization for 1800C is the closest to 1 ($0.78^{+0.07}_{-0.09}$). However, this model gives a SNR radius that is a factor of ~ 2 too small. A simple way of resolving this discrepancy is to assume that the SNR is a factor of ~ 2 closer than expected, without changing the ambient density. The surface brightness and physical size of the SNR would be unaffected, while the apparent size of the SNR would be ~ 2 times greater, and in better agreement with the observed size of the arc. This suggested resolution requires the height at which $n_0 = 0.005 \text{ cm}^{-3}$ to be $\approx 1 \text{ kpc}$, as opposed to 1.8 kpc . Is a density of 0.005 cm^{-3} at $z = 1 \text{ kpc}$ plausible?

The density model $n_0(z)$ used by Shelton (2006) comes from Ferrière (1998). At $z = 1 \text{ kpc}$, this model gives $n_0(\text{H} + \text{He}) = 0.016 \text{ cm}^{-3}$, assuming 10% He by number. This density is dominated by the neutral medium (37%) and the warm ionized medium (61%), the remaining 2% being due to the hot ionized medium. Ferrière's model for the warm ionized medium comes from the distribution of free electrons derived by Cordes et al. (1991), while her model for the neutral medium comes from Dickey & Lockman (1990).

We used a Monte Carlo method to investigate whether or not a density of 0.005 cm^{-3} at $z = 1 \text{ kpc}$ was plausible. For each trial, we randomly varied each parameter of the warm-ionized and neutral models according to its error bar, and calculated $n_0(z = 1 \text{ kpc})$ from the resulting density model. Dickey & Lockman (1990) do not quote errors for the neutral model's parameters, so we assumed 50% errors. We included the hot ionized medium in $n_0(z)$, but did not vary its model parameters. We carried out 100,000 trials. Approximately 24% of the trials were discarded because the random number generator gave one or more negative (and hence unphysical) model parameters for those trials. Of the remaining trials, 7% gave a density $n_0(z = 1 \text{ kpc}) \leq 0.005 \text{ cm}^{-3}$. We therefore cannot rule out the possibility that the density at $z = 1 \text{ kpc}$ is as low as 0.005 cm^{-3} , corresponding to model 1800C. As a result, we cannot rule out the possibility that the arc is well-described by model 1800C at $z \sim 1 \text{ kpc}$ instead of $z = 1.8 \text{ kpc}$, although this model is a less favored option.

The models with $E_0 = 0.5 \times 10^{51} \text{ erg}$ for $z = 850 \text{ pc}$ (850A, 850B, 850C) are in better agreement with the observed radius of the arc, but they are a factor of ~ 3 too bright. As stated above, the surface brightness of a model SNR depends on the density of the ambient medium. However, as the emission is dominated by line emission from ionized metals, the SNR surface brightness also depends upon the metallicity of that medium. If the metallicity of the interstellar medium above the disk were a factor of ~ 3 lower than our assumed value (Anders & Grevesse 1989), the model SNR surface brightness would be in better agreement with that of the arc. We also note that uncertainties in the model line emissivities may be important, although this is more difficult to quantify.

The halo gas-phase abundances of Si, Mg, and Fe, which are all important line emitters in the $1/4 \text{ keV}$ band, are ~ 0.6 , ~ 0.3 , and ~ 0.2 solar (Savage & Sembach 1996, using Anders & Grevesse 1989 as a reference). However, these values do not imply a subsolar metallicity for the halo; instead, these elements are assumed to be depleted on to dust. In contrast, S has a solar gas-phase abun-

dance in the halo (Savage & Sembach 1996), implying it is not depleted on to dust. Also, the abundance of Ne (which, being a noble gas, is not expected to be depleted) toward an X-ray binary (4U 1820–303) at $z \approx 1 \text{ kpc}$ is 1.2 ± 0.2 solar (Yao & Wang 2006). (However, this source is at low Galactic latitude [$b = -7.91^\circ$], so the sightline samples the disk as well as the halo.)

These measurements suggest that the halo has a solar metallicity, at least for $z \lesssim 2 \text{ kpc}$. However, the X-ray emission from a halo SNR depends upon the gas-phase metallicity in the shock-heated gas. Whether or not this metallicity is subsolar depends on how quickly the dust is destroyed behind the shock. In gas of temperature $T = 1 \times 10^6 \text{ K}$ and density n , the rate of change of a dust grain's radius a due to thermal sputtering is (Seab 1987)

$$\frac{da}{dt} \sim 10^{-3} \left(\frac{n}{\text{cm}^{-3}} \right) \text{ \AA yr}^{-1}, \quad (1)$$

and so the lifetime τ of a dust grain in the gas is

$$\tau \equiv \frac{a}{da/dt} \sim 10^6 \left(\frac{a}{100 \text{ \AA}} \right) \left(\frac{0.1 \text{ cm}^{-3}}{n} \right) \text{ yr}. \quad (2)$$

The density $n = 0.1 \text{ cm}^{-3}$ used in the above expression is the approximate density in the immediate post-shock region of the SNR models at $z = 850 \text{ pc}$; this region is where most of the X-ray emission originates. The lifetime of a 100-\AA dust grain in such a SNR is an order of magnitude greater than the SNR age given by our spectral analysis ($\sim 10^5 \text{ yr}$), and dust grains larger than 100 \AA would survive even longer. We would therefore expect that the X-ray emission from a young halo SNR would reflect the depleted gas-phase abundances in Savage & Sembach (1996), not the total halo abundances.

The effect that these depleted abundances would have on our model SNR spectra depends on the details of which elements are depleted and by how much. However, as the gas-phase halo abundances of several elements are $\sim 1/3$ solar (Savage & Sembach 1996), it seems reasonable to suggest that our model SNR spectra, calculated using Anders & Grevesse (1989) abundances, may be a factor of ~ 3 too bright. Using a metallicity of $\sim 1/3$ solar for a SNR with $E_0 = 0.5 \times 10^{51} \text{ erg}$ at $z = 850 \text{ pc}$ ($n_0 = 0.02 \text{ cm}^{-3}$) would bring the model SNR surface brightness into better agreement with that of the arc. If the arc is a young extraplanar SNR whose X-ray-emitting gas has a metallicity of $\sim 1/3$ solar, our analysis would then favor a height $z \sim 1 \text{ kpc}$ for the arc, as a SNR at greater height (lower ambient density) would have too low a surface brightness, as well as being too small.

5.2.2. The Morphology of the Arc

As noted in §4.4, the observed radial width of the arc is larger than that predicted by our SNR model. We investigated this discrepancy by looking for known Galactic SNRs at an analogous stage in their evolution (i.e. roughly half way to the formation of the cool shell), in order to see how their observed X-ray morphologies compared with our model.

We carried out a SNR simulation with $E_0 = 0.5 \times 10^{51} \text{ erg}$, $B_{\text{eff}} = 0$ (model type A), with an ambient density ($n_0 = 2 \text{ cm}^{-3}$) representative of the disk, rather

than the halo. From this simulation, we estimated that a $\sim 15,000$ -yr old SNR in the disk would be at a similar stage in its evolution as our best-fitting halo SNR model for the arc. We found that the Vela SNR (G263.9–3.3) provides a good analog to the arc: based on the apparent origin of X-ray-emitting explosion fragments beyond the blastwave and the proper motion of the Vela pulsar (PSR B0833–45), Aschenbach et al. (1995) estimated the age of the remnant to be $18,000 \pm 9,000$ yr, consistent with the pulsar’s spin-down age of 11,000 yr (Taylor et al. 1993).

As with the analogous models of halo SNRs, the new simulation with $n_0 = 2 \text{ cm}^{-3}$ predicts that a SNR of the age of Vela would have an X-ray-bright rim whose width is $\sim 1/10$ of the radius of the SNR (cf. Figs. 5 and 9). In contrast, Vela exhibits an asymmetrical bright rim to the north and east whose width is \sim half the remnant radius (Aschenbach et al. 1995).

Our SNR models underpredict the widths of the arc and of the Vela SNR’s X-ray-bright rim. These discrepancies may be due to the limitations of our SNR simulations, which are one-dimensional, and assume a uniform ambient density and a uniform non-thermal pressure in the radial direction. Three-dimensional simulations could include non-uniform ambient densities and different magnetic field geometries, which could affect the predicted X-ray morphology. Such simulations could also simulate hydrodynamical instabilities, which would broaden the apparent width of the arc. E. Raley (2009, private communication) has provided us with the results of a 3-D simulation of a SNR with $E_0 = 0.5 \times 10^{51}$ erg evolving in zero magnetic field at $z = 400$ pc (see also Raley et al. 2007). Using these results, K. Kwak (2009, private communication) has provided us with spectra calculated for various sightlines across the remnant, assuming CIE. For a young remnant, the 3-D model does indeed predict a broader X-ray-bright rim than the 1-D model. However, the 1-D SNR models that we used include self-consistent modeling of the ionization evolution, which we used to calculate non-equilibrium X-ray spectra. Developing a 3-D SNR model that includes ionization evolution is beyond the scope of this paper.

We conclude this discussion of the arc’s morphology by noting that the arc does not trace a full circle. Such asymmetries are not uncommon in SNRs (see, e.g., the collection of SNR images at the *ROSAT* Guest Observer Facility¹⁰ and the *Chandra* Supernova Remnant Catalog¹¹). The arc’s asymmetry may be due to a non-uniform ambient medium and/or a complicated magnetic field geometry, both of which are beyond the reach of our 1-D simulations.

5.2.3. Non-X-ray Observations, and Future X-ray Observations

We have considered further ways in which we could test the hypothesis that the arc is the edge of an extraplanar SNR. Our X-ray spectral analysis implies that, if the arc is a SNR, then it is young, in the sense that it has not yet formed a dense cool shell. This is unfortunate, as it means we do not expect H α emission due to recombination in the cooling shell, nor H I emission from the gas

that has already cooled. The Southern H α Sky Survey Atlas (SHASSA; Gaustad et al. 2001; Finkbeiner 2003) shows no sign of an H α -emitting shell around the arc.

The hydrodynamical SNR models that we have used in our spectral analysis also make predictions for the column densities of various highly ionized metals (e.g., N V, O VI, O VII, O VIII). In principle, therefore, far-ultraviolet and X-ray absorption line spectroscopy could be used to test the results of our spectral analysis. Unfortunately, in practice it would be extremely difficult to detect unambiguously an enhanced ion column density due to an extraplanar SNR, given the sparsity of stars in this region.

Table 5 shows various ion column densities predicted for a 100,000-yr old SNR at $z \geq 850$ pc with $E_0 = 0.5 \times 10^{51}$ erg. The predicted column density is dependent upon z and B_{eff} : models at lower z (and hence higher ambient density) or with larger B_{eff} give larger column densities. Table 5 shows the range of values predicted by the various models. The N V and O VI columns (and, to a lesser extent, the O VII column) are peaked at the edge of the remnant (see Figs. 8 and 9 in Shelton 1998; that model corresponds to our model 1300B). For these ions, Table 5 shows both the peak column, and the column in the SNR interior. The O VIII column does not peak at the edge of the SNR.

Table 5 also shows the range of column densities observed in multiple directions across the sky. In general, the column densities predicted by the SNR are smaller than the spread in the observed column densities, and so an increased column density in the vicinity of the arc could not be unambiguously attributed to an extraplanar SNR. Furthermore, the predicted O VII columns are of the same order of magnitude as the errors on the O VII measurements. Some of the models (with $z = 850$ pc) predict peak N V and O VI column densities near the remnant edge that are significantly larger than the variation across the sky. However, observing these large column densities would require a fortuitously positioned background source. In general, using absorption line spectroscopy to test whether or not the arc is the edge of an extraplanar SNR would require column density measurements from several different sightlines on and around the arc.

Perhaps the best way of further testing the hypothesis that the arc is the edge of an extraplanar SNR will be with future, higher-resolution X-ray spectrometers. Although our *Suzaku* spectra are consistent with CIE models, it is possible that higher resolution spectra could reveal unambiguous signs of non-equilibrium ionization that we would expect behind the blastwave of a young extraplanar SNR. Sensitivity in the 1/4 keV band, where the arc is bright, but where we currently only have the low-resolution *ROSAT* R12 data, would be particularly useful.

5.3. Other extraplanar SNRs?

Shelton et al. (2007) and Lei et al. (2009) have analyzed the halo O VI and X-ray emission in the direction $l \approx 279^\circ$, $b \approx -47^\circ$, which samples an X-ray-bright region visible in the 1/4-keV RASS maps. They used a nearby ($d = 230$ pc) shadowing filament to separate the foreground (LB/SWCX) and background (halo) emission. This filament is visible toward the upper-right cor-

¹⁰ <http://heasarc.nasa.gov/docs/rosat/gallery/snrs.html>

¹¹ <http://hea-www.cfa.harvard.edu/ChandraSNR/>

TABLE 5
PREDICTED SNR ION COLUMN DENSITIES AND OBSERVED ION COLUMN DENSITIES

Ion	Predicted SNR Column Density		Observations		
	Peak (10^{14} cm^{-2})	Interior (10^{14} cm^{-2})	Column Density (10^{14} cm^{-2})	Number of Sightlines	Ref.
N V	0.2–1.6	0.03–0.19	0.57 ± 0.36^a	9	1
O VI	3.9–14.2	0.6–2.1	2.5 ± 1.0^a	91	2
O VII	13–43	10–23	~ 100 –200	3	3,4,5
O VIII	...	1.3–8.5	~ 10 –100	2	3,4

REFERENCES. — (1) Sembach & Savage 1992; (2) Savage et al. 2003; (3) Yao & Wang 2007a; (4) Yao & Wang 2007b; (5) Yao et al. 2008.

NOTE. — The predicted column densities are from 100,000-yr old SNRs at $z \geq 850$ pc with $E_0 = 0.5 \times 10^{51}$ erg. The observed values indicate the variation in the column densities detected from multiple sightlines over the sky.

^a Mean \pm standard deviation

ner of Figure 1.

Shelton et al. (2007) showed that the O VI-to-1/4 keV emission ratio was a good age diagnostic for an extraplanar SNR. For the halo beyond the shadowing filament, they found that this ratio was consistent with that from a $\sim 40,000$ –70,000-yr old SNR with $n_0 = 0.01 \text{ cm}^{-3}$, $E_0 = 0.5 \times 10^{51}$ erg, $B_{\text{eff}} = 2.5 \mu\text{G}$ (model 1300B in Table 3). More generally, they found that if the hot gas that they observed can be compared to that in an undisturbed extraplanar SNR, the time since heating is $\sim 10^4$ – 10^5 yr.

Using a combination of *Suzaku*, *ROSAT* R12, and *FUSE* O VI data, Lei et al. (2009) constructed a differential emission measure (DEM) model for the halo beyond the shadowing filament. Their DEM is a broken power-law between $T \sim 10^5$ K and $T \sim 10^7$ K, with a break at $T_{\text{break}} \sim 10^6$ K. They suggest that the lower-temperature part of the DEM ($T < T_{\text{break}}$) is due to an extraplanar SNR. The O VI and soft X-ray intensities of this lower-temperature component are best matched by a $\sim 180,000$ -yr old SNR with $n_0 = 0.02 \text{ cm}^{-3}$ ($z = 850$ pc). Given the uncertainties in the modeling, Shelton et al. (2007) and Lei et al. (2009) obtained consistent results: both studies found that the O VI and 1/4 keV X-ray emission from the halo beyond the shadowing filament are consistent with the emission from a pre-shell-formation SNR at $z \sim 1$ kpc.

Shelton (2006) predicted that there would be approximately one bright, pre-shell-formation SNR per hemisphere at high-latitudes. Our arc analysis and the analysis of the filament region (Shelton et al. 2007; Lei et al. 2009) suggest the presence of two halo SNRs at similar heights and of similar ages in the southern Galactic hemisphere. Given the uncertainties in the computer simulations and SN rate, this result should not be considered a refutation of Shelton’s (2006) prediction. However, given this result, we expect that most other directions in the southern Galactic hemisphere would not exhibit the properties of young, extraplanar SNRs. This could be tested by measuring the O VI-to-1/4 keV ratio for a large number of high-latitude directions.

6. SUMMARY

We have analyzed a set of three *Suzaku* spectra obtained from pointings on and around a bright arc that appears in the 1/4 keV soft X-ray background at $l \approx 247^\circ$, $b \approx -64^\circ$, and have tested the hypothesis that the arc is the edge of an extraplanar SNR. For this purpose we

have used spectral models generated from 1-D hydrodynamical simulations of SNRs at a variety of heights above the disk. We also supplemented our *Suzaku* spectra at lower energies with *ROSAT* R12 (1/4 keV) data.

The three *Suzaku* + R12 spectra and the observed size of the arc are reasonably well explained by a model in which the arc is the bright edge of a $\sim 100,000$ -yr old SNR at a height $z \sim 1$ –2 kpc (ambient density $n_0 = 0.02$ – 0.005 cm^{-3}), blown by a supernova with $E_0 = 0.5 \times 10^{51}$ erg. The remnant is still in the adiabatic stage of its evolution, having not yet formed a cool shell.

The agreement between the model and the observations is not perfect: the models are generally either a few times too bright, or a factor of ~ 2 too small. The agreement between the model and the observations can be improved if the metallicity of the X-ray-emitting gas is $\sim 1/3$ solar. Such a subsolar metallicity is plausible, as metals depleted on to dust are unlikely to have been returned to the gas phase within the $\sim 100,000$ -yr lifetime of the remnant. If the metallicity is $\sim 1/3$ solar, this scenario would favor $z \sim 1$ kpc for the arc, as higher remnants would be too faint and too small.

The radial width of the arc is underpredicted by our SNR model. The Vela SNR, a known remnant in the Galactic disk, appears to be at a similar stage in its evolution as our arc SNR model. Like the arc, its X-ray-bright rim is much wider than that predicted by our simulations. We suggest that this discrepancy could be due to the 1-D nature of the simulations, as well as assumptions of uniform ambient density and non-thermal pressure. Higher-dimensional hydrodynamical simulations may better explain the morphology of the arc, but are beyond the scope of this study.

It should be noted that we have not tested other scenarios for the arc’s formation, and also that equilibrium models provide good fits to the *Suzaku* spectra. However, we conclude by echoing Shelton (2006), and note that the extraplanar SNR scenario discussed here provides a good explanation for an arc-shaped enhancement in the high-latitude soft X-ray background. If this scenario is correct, it supports the idea that extraplanar supernovae contribute to the heating of the hot halo gas.

We would like to thank Steve Snowden for helpful comments regarding HEASARC’s X-ray Background Tool, Liz Raley for helpful discussions on fitting the

SNR spectral models to the data and for supplying the 3-D SNR simulation mentioned in §5.2.2, and Kyujin Kwak for calculating X-ray spectra from said simulation. We also thank the referee, whose comments have helped improve this paper. This research has made use of data obtained from the *Suzaku* satellite, a collaborative mission between the space agencies of

Japan (JAXA) and the USA (NASA). The OMNI data were obtained from the GSFC/SPDF OMNIWeb interface at <http://omniweb.gsfc.nasa.gov>. This research was funded by NASA grants NNH06ZDA001B-SUZ2 and NNX08AZ83G, awarded through the *Suzaku* Guest Observer Program.

REFERENCES

- Anders, E., & Grevesse, N. 1989, *Geochim. Cosmochim. Acta*, 53, 197
- Arnaud, K. A. 1996, in *ASP Conf. Ser. 101: Astronomical Data Analysis Software and Systems V*, ed. G. H. Jacoby & J. Barnes, 17
- Aschenbach, B., Egger, R., & Trümper, J. 1995, *Nature*, 373, 587
- Bałucińska-Church, M., & McCammon, D. 1992, *ApJ*, 400, 699
- Breitschwerdt, D., & Schmutzler, T. 1994, *Nature*, 371, 774
- Burrows, D. N., & Mendenhall, J. A. 1991, *Nature*, 351, 629
- Chen, L.-W., Fabian, A. C., & Gendreau, K. C. 1997, *MNRAS*, 285, 449
- Cordes, J. M., Weisberg, J. M., Frail, D. A., Spangler, S. A., & Ryan, M. 1991, *Nature*, 354, 121
- Cravens, T. E. 2000, *ApJ*, 532, L153
- Cravens, T. E., Robertson, I. P., & Snowden, S. L. 2001, *JGR*, 106 (A11), 24883
- Dickey, J. M., & Lockman, F. J. 1990, *ARA&A*, 28, 215
- Ferrière, K. 1998, *ApJ*, 497, 759
- Finkbeiner, D. P. 2003, *ApJS*, 146, 407
- Fujimoto, R., et al. 2007, *PASJ*, 59, S133
- Galeazzi, M., Gupta, A., Covey, K., & Ursino, E. 2007, *ApJ*, 658, 1081
- Gaustad, J. E., McCullough, P. R., Rosing, W., & Van Buren, D. 2001, *PASP*, 113, 1326
- Henley, D. B., & Shelton, R. L. 2008, *ApJ*, 676, 335
- Ishisaki, Y., et al. 2007, *PASJ*, 59, S113
- Kalberla, P. M. W., Burton, W. B., Hartmann, D., Arnal, E. M., Bajaja, E., Morras, R., & Pöppel, W. G. L. 2005, *A&A*, 440, 775
- Koutroumpa, D., Acero, F., Lallement, R., Ballet, J., & Kharchenko, V. 2007, *A&A*, 475, 901
- Koutroumpa, D., Lallement, R., Kharchenko, V., Dalgarno, A., Pepino, R., Izmodenov, V., & Quémerais, E. 2006, *A&A*, 460, 289
- Koyama, K., et al. 2007, *PASJ*, 59, S23
- Kuntz, K. D., & Snowden, S. L. 2000, *ApJ*, 543, 195
- Lei, S., Shelton, R. L., & Henley, D. B. 2009, *ApJ*, in press (arXiv:0906.1532v1)
- Mitsuda, K., et al. 2007, *PASJ*, 59, S1
- Norman, C. A., & Ikeuchi, S. 1989, *ApJ*, 345, 372
- Raley, E. A., Shelton, R. L., & Plewa, T. 2007, *ApJ*, 661, 222
- Rasmussen, J., Sommer-Larsen, J., Pedersen, K., Toft, S., Benson, A., Bower, R. G., & Grove, L. F. 2009, *ApJ*, 697, 79
- Raymond, J. C., & Smith, B. W. 1977, *ApJS*, 35, 419
- Robertson, I. P., & Cravens, T. E. 2003a, *JGR*, 108 (A10), 8031
- . 2003b, *GeoRL*, 30(8), 1439
- Savage, B. D., & Sembach, K. R. 1996, *ARA&A*, 34, 279
- Savage, B. D., et al. 2003, *ApJS*, 146, 125
- Schlegel, D. J., Finkbeiner, D. P., & Davis, M. 1998, *ApJ*, 500, 525
- Seab, C. G. 1987, in *Interstellar Processes*, ed. D. J. Hollenbach & H. A. Thronson, Jr. (Dordrecht: Reidel), 491
- Sembach, K. R., & Savage, B. D. 1992, *ApJS*, 83, 147
- Shapiro, P. R., & Field, G. B. 1976, *ApJ*, 205, 762
- Shelton, R. L. 1998, *ApJ*, 504, 785
- . 1999, *ApJ*, 521, 217
- . 2006, *ApJ*, 638, 206
- Shelton, R. L., Sallmen, S. M., & Jenkins, E. B. 2007, *ApJ*, 659, 365
- Smith, R. K., et al. 2007, *PASJ*, 59, S141
- Smith, R. K., Brickhouse, N. S., Liedahl, D. A., & Raymond, J. C. 2001, *ApJ*, 556, L91
- Snowden, S. L., Collier, M. R., & Kuntz, K. D. 2004, *ApJ*, 610, 1182
- Snowden, S. L., Egger, R., Finkbeiner, D. P., Freyberg, M. J., & Plucinsky, P. P. 1998, *ApJ*, 493, 715
- Snowden, S. L., et al. 1997, *ApJ*, 485, 125
- Snowden, S. L., Freyberg, M. J., Kuntz, K. D., & Sanders, W. T. 2000, *ApJS*, 128, 171
- Snowden, S. L., et al. 1995, *ApJ*, 454, 643
- Snowden, S. L., Mebold, U., Hirth, W., Herbstmeier, U., & Schmitt, J. H. M. M. 1991, *Science*, 252, 1529
- Spitzer, L. 1978, *Physical Process in the Interstellar Medium* (New York: Wiley)
- Taylor, J. H., Manchester, R. N., & Lyne, A. G. 1993, *ApJS*, 88, 529
- Toft, S., Rasmussen, J., Sommer-Larsen, J., & Pedersen, K. 2002, *MNRAS*, 335, 799
- Winkler, P. F., Gupta, G., & Long, K. S. 2003, *ApJ*, 585, 324
- Yan, M., Sadeghpour, H. R., & Dalgarno, A. 1998, *ApJ*, 496, 1044
- Yao, Y., Nowak, M. A., Wang, Q. D., Schulz, N. S., & Canizares, C. R. 2008, *ApJ*, 672, L21
- Yao, Y., & Wang, Q. D. 2005, *ApJ*, 624, 751
- . 2006, *ApJ*, 641, 930
- . 2007a, *ApJ*, 658, 1088
- . 2007b, *ApJ*, 666, 242
- Yoshino, T., et al. 2009, *PASJ*, submitted (arXiv:0903.2981v1)